ORIGINAL ARTICLE



Radial tool wear analysis and compensation strategy for microhole arrays in sequential hybrid laser beam micromachining (LBMM) and micro-EDM

Wan Ahmad Bin Wan Azhar¹ · Tanveer Saleh¹

Received: 29 March 2025 / Accepted: 27 September 2025 © The Author(s) 2025

Abstract

Microhole arrays have significant applications across various industries, including aerospace, turbo machinery, industrial filtration, microfluidic devices, and biomedical engineering. Several methods exist for manufacturing microhole arrays, but the sequential hybrid laser beam micromachining (LBMM) and microelectrical discharge machining (μ EDM) process offers complementary advantages, significantly reducing production time while achieving high precision. However, due to the pre-existing tapered holes created by LBMM, tool wear during the subsequent μ EDM process primarily occurs on the sides of the electrode, leading to more significant radial wear. Reusing the same electrode results in tapered holes, while frequent electrode replacement is impractical and costly. This study investigates the tool wear characteristics in the hybrid LBMM- μ EDM process across different materials and thicknesses and proposes compensation strategies to improve machining consistency. Axial and radial tool wear lengths were characterized by machining 300- μ m microhole arrays on 600 and 200- μ m thick copper and stainless steel workpieces, with microscopic images of the electrode captured after each machining step. Analysis revealed that the hybrid LBMM- μ EDM process resulted in more prominent radial tool wear length compared to the pure μ EDM process, while the pure μ EDM process exhibited higher axial tool wear length. Radial wear was more pronounced in stainless steel than in copper, and thicker workpieces increased axial wear. To address tapering, a compensation strategy was developed by adjusting the programmed depth based on radial wear, reducing the taper angle by 7 × . This approach enables the hybrid process to match the hole quality of pure μ EDM while achieving a 4 × faster machining rate.

 $\textbf{Keywords} \ \ LBMM \cdot Laser \cdot Micromachining \cdot Micro-EDM \cdot Microhole \ array \cdot Electrical \ discharge \ machining \cdot Hybrid \cdot Tool \ wear \cdot Compensation \cdot Sequential$

1 Introduction

Microhole arrays are essential in a wide range of industries. In aerospace applications, microhole arrays such as film cooling holes (FCHs) are critical for enhancing turbine blade cooling and thermal protection [1, 2]. Recent studies have demonstrated the feasibility of machining microhole arrays on Cf-ZrB₂-SiC, a next-generation aerospace composite material [3]. In industrial filtration, they improve heavy metal detection in water through organic membranes [4]. In

and biocompatible microhole arrays regulate fluid flow and enable controlled drug release [5, 6]. Recent studies have explored the use of microhole arrays in microarray patches (MAPs) for targeted drug delivery and biosensing applications [7]. Moreover, microholes fabricated in PDMS polymers are particularly advantageous for these biomedical uses due to the material's low toxicity, optical transparency, and biocompatibility, enabling safe and effective interaction with biological tissues [8]. In addition, microholes are crucial in biomedical applications such as biochip fabrication, where they are replicated on glass substrates using micromolded pin arrays [9]. Microhole arrays on superhydrophobic surfaces enable self-cleaning and drag reduction [10]. In optoelectronics, silicon microhole arrays enhance optical absorption, benefiting advanced solar cells [11]. In printing, inkjet

nozzles rely on microhole arrays (50-µm diameter, 169-µm

microfluidics and biomedical applications, ceramic (ZrO₂)

Published online: 04 November 2025



[☐] Tanveer Saleh tanveers@iium.edu.my

Autonomous Systems and Robotics Research Unit, Department of Mechatronics Engineering, International Islamic University Malaysia, Jalan Gombak, 53100 Kuala Lumpur, Malaysia

pitch) for high-resolution output [12]. Graphene-based microhole arrays improve heat transfer and thermoelectric efficiency, supporting energy conversion and fuel cell performance by optimizing gas diffusion and reaction kinetics [13, 14]. The precise manufacturing of these structures ensures their reliability and effectiveness across these applications.

Various techniques are used to manufacture microhole arrays, including electrochemical machining (ECM), chemical etching, mechanical punching, microelectrical discharge machining (µEDM), laser drilling, ultrasonic machining, and abrasive jet machining [15]. ECM offers high material removal rates (MRRs) and excellent surface quality but requires precise control and long production setup times [16]. When using non-Newtonian polyacrylamide electrolytes, ECM has created microhole arrays in stainless steel (SS304) with an average diameter of 330.11 µm and a depthto-diameter ratio of 0.048 [17]. Chemical etching is costeffective but can cause undercutting, temperature sensitivity, and environmental concerns. Mechanical punching is productive and cost-efficient but is limited by hole size and alignment challenges. Using punching without die technology, an array of 37 tapered microholes was successfully fabricated in aluminum alloy (Al6061) with a depth of 260 µm, demonstrating its potential for high aspect ratio holes [18]. In addition, µEDM is precise for hard materials but is limited to conductive materials and slower speeds, as seen in stainless steel holes with diameters of 18.91 µm and an aspect ratio of 142 [19]. Laser drilling is fast and ideal for high aspect ratios but may cause heat-affected zones (HAZs) and be costly. A two-step femtosecond laser method achieved microholes in Inconel 718 with near-zero taper and high aspect ratios [20]. Ultrasonic machining is versatile for complex shapes but suffers from high tool wear and microcracks. Abrasive jet machining is cost-effective for brittle materials but can lead to tapered holes. The choice of method depends on material properties, hole specifications, and production goals.

Researchers have explored hybrid machining methods to improve micromachining performance by combining different processes to overcome individual limitations. In laserassisted micromilling, the laser enhances material removal by heating the workpiece, increasing MRRs by up to six times [21]. A laser–electrochemical hybrid polishing process has also been studied to improve surface quality in selectively laser melted 316L stainless steel, yielding crack-free surfaces and enhanced wear resistance [22]. Another development integrates laser technology with µEDM, where laser beam micromachining (LBMM) is used for rough machining to minimize HAZs and improve dimensional accuracy, followed by µEDM for fine finishing. This hybrid method has reduced machining time by up to 90% and improved hole quality compared to conventional µEDM [23, 24]. Other research observed a 50-60% decrease in machining time with the hybrid method, without compromising hole quality, compared to standard μEDM [25]. The hybrid approach also significantly reduces machining time, with LBMM drilling a 10-mm thick sample in just 3 s compared to 48 s with μEDM , while producing smaller recast layers [26].

One of the remaining challenges in µEDM is the prominence of tool wear. Extensive literature has been developed to study tool wear in µEDM throughout the years. A 2D geometric simulation model was developed to predict electrode wear during µEDM drilling of through-hole arrays, showing prediction errors within 5 µm for total wear and 15 μm for axial wear, improving diameter consistency by 8.02% [27]. Another study optimized pulse generator parameters to reduce electrode wear, achieving a standard deviation of $0.15 \mu m$ for a 16×16 microhole array, with smaller arrays showing similar improvements [28]. Research has also identified factors like spark discharge energy [29], machining stability [30], and piezoelectric self-adaptive µEDM [31] as influencing wear. Compensation strategies, including predictive and real-time approaches, have been developed to enhance machining accuracy and efficiency, such as 3D grid-based models [32], electrothermal models for blind hole machining [33], robust control to maintain machining gap [34], and real-time shape-based compensation [35]. Significant progress has been made in detecting and compensating for electrode wear, improving both accuracy and efficiency.

In the LBMM-µEDM process, the pre-existing hole created by the LBMM leads to different tool wear characteristics compared to pure µEDM process. Due to the tapered prehole created by LBMM, tool wear during µEDM is predominantly observed on the sides of the electrode, leading to more significant radial wear length compared to axial wear length. However, there is limited literature that investigates this distinction and its implications in detail. A recent study investigated the behavior of µEDM drilling on preholes to improve process performance and machining accuracy [36]. Titanium alloy sheets were used with electrode diameters of 300 µm to evaluate the effects of prehole diameter, electrode type, centering accuracy, and hole depth. Results showed that preholes significantly enhance performance compared to traditional EDM drilling due to reduced debris contamination in the machining zone. Increasing the prehole size caused minimal changes in MRR. The electrode type (cylindrical or tubular) influenced only the geometrical characteristics, not process performance. Misalignment of the final hole on the prehole improved debris flow and efficiency but only when part of the prehole remained outside the final hole. Within the experimental limits, hole depth had no effect on the results. Furthermore, similar studies show that the primary factor improving drilling efficiency in the hybrid process is not the material removal by the laser but the predrilled hole's role in aiding debris and bubble exclusion during µEDM [24]. The study confirms this claim by



demonstrating that upsetting the laser-drilled hole facilitates debris and bubble removal in deep-hole μEDM by enlarging the exit diameter.

As far as the authors are aware, no studies have yet investigated the tool wear characteristics of µEDM in the sequential hybrid LBMM-µEDM process. Although µEDM produces high-quality microholes with good dimensional accuracy, its machining speed is relatively slow. To overcome this limitation, the sequential hybrid LBMM-µEDM approach is used, combining the fast material removal capability of LBMM with the precision of µEDM. However, tool wear in the sequential hybrid LBMM-µEDM process continues to be a concern, particularly for the fabrication of a microhole array. If tool wear can be effectively compensated while maintaining a high machining rate, this sequential hybrid process can achieve both speed and accuracy in microhole fabrication. Moreover, reusing the same electrode for subsequent holes causes tapering in the microholes, while frequent electrode replacement is impractical. Additionally, cumulative wear becomes significant when drilling arrays of microholes, particularly in thicker materials and varying material types.

This paper explored the µEDM tool wear characteristics in the sequential hybrid LBMM-µEDM process and developed compensation strategies to improve machining consistency for microhole array fabrication. The axial and radial wear length of the microelectrode was characterized by machining 300-µm diameter microhole arrays on 600 and 200-µm thick copper and stainless steel workpieces. Using a microscopic camera, images of the microelectrode were captured after each machining step, allowing for precise measurements of axial and radial wear length. Based on these findings, a compensation strategy was proposed to calculate the required machining depth and mitigate the impact of tapering on the quality of successive microhole arrays while maintaining fast processing speed.

2 Materials and methods

This section details the experimental setup used to investigate axial and radial wear length on the hybrid LBMM-µEDM process, including the specific equipment and procedures employed. Additionally, the characterization techniques used to assess the performance and precision of the system are outlined, offering a comprehensive understanding of the experimental procedures and evaluation.

2.1 Hybrid LBMM-µEDM setup

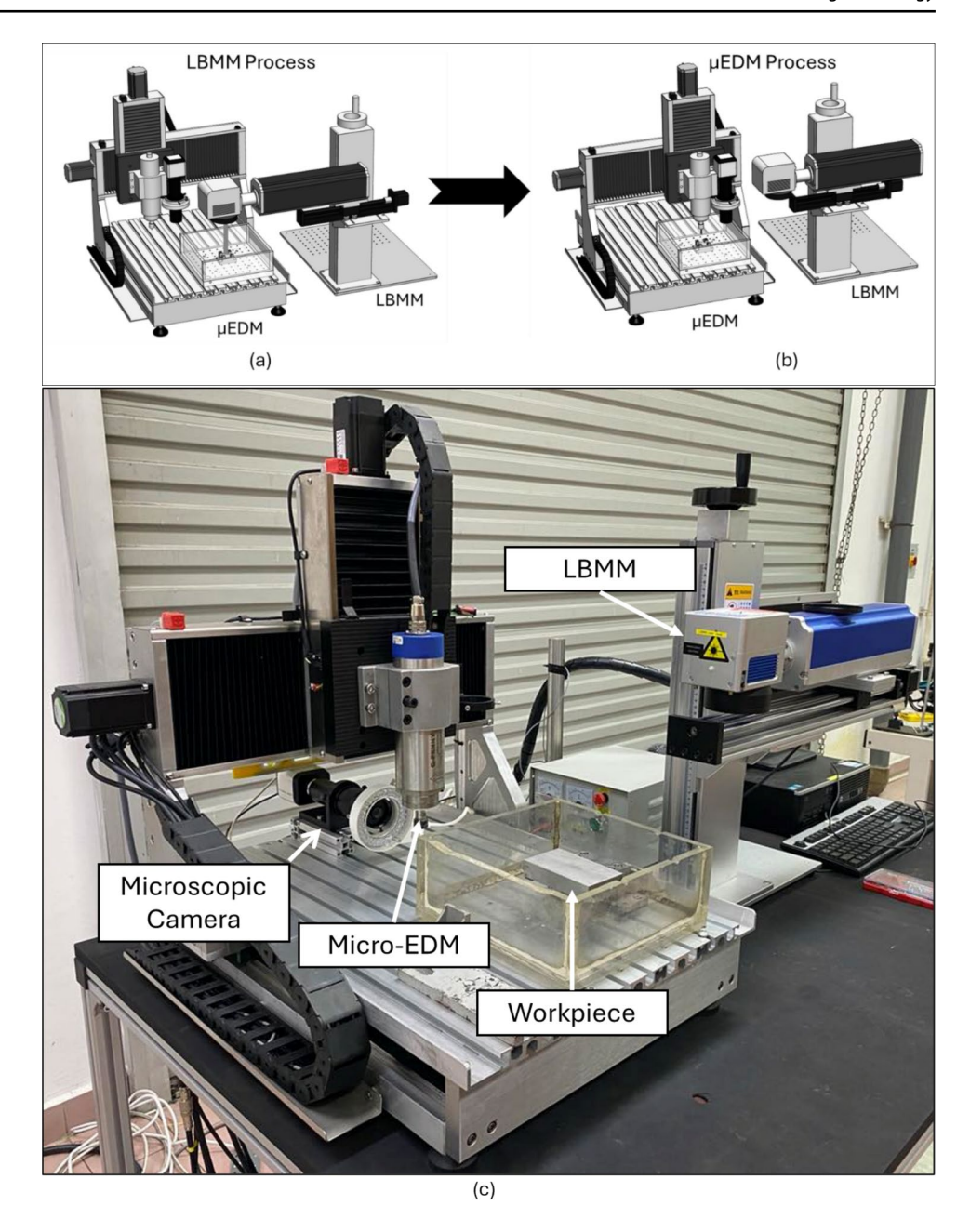
The integrated LBMM and μ EDM system, developed in-house [37], features the LBMM system positioned horizontally offset from the μ EDM setup. The workpiece remains within the μ EDM workspace, accessible for

both processes. The LBMM system features a 50-W fiber laser (1060-nm wavelength, 50-µm spot size, 200-mm focal length) controlled by an X/Y galvanometer scanner with ± 15° scan angle and 12-µrad resolution. Laser power was calibrated using a Gentec Pronto-250 power meter, which measures average output power. The calibration was performed across a range of 10% to 100% laser settings. Although the laser is rated at 50 W, the actual output at 100% was approximately 38.6 W. This represents a power loss of about 22.8%, which aligns with the data provided by the supplier of this fiber laser system. This loss occurs because the laser beam passes through several optical elements such as collimators, beam expanders, mirrors, and the galvanometric scanner before exiting the system. Each optical component contributes to reflection, scattering, or absorption losses, resulting in reduced power delivered to the workpiece surface. A calibration curve was established to map the percentage settings to actual output power. For this experiment, the laser was set to 90%, corresponding to a calibrated power of 35.4 W. The laser head is heightadjustable via a rotary handle and moves horizontally on a motorized linear stage, with process parameters managed through EZCAD Lite software. The µEDM setup, a threeaxis CNC machine with 15-µm repeatability, operates in the same workspace and includes a µEDM spindle and microscopic camera mounted on the Z-axis plate. Custom software handles camera viewing, parameter adjustment, G-code execution, and axis monitoring. Figure 1 illustrates the machine configuration: during LBMM (Fig. 1a), the laser head positions above the workpiece; after retracting, the µEDM system moves in for machining (Fig. 1b), with the transition taking 36 s.

A microscopic camera, mounted on the µEDM machine, is used to establish a common coordinate system for both the camera and the µEDM electrode [37], as depicted in Fig. 1a,b. During the calibration process, a blind reference hole is machined using µEDM at known coordinate positions. The microscopic camera is then moved using the CNC stages to align its crosshair overlay with the center coordinates of the reference hole. The x and y deviations, representing the offset distances between the electrode and the camera crosshair, are determined using linear scale feedback. These offset distances are subsequently utilized by the μEDM machine to transition seamlessly between the camera view and precise electrode alignment. Additionally, a second microscopic camera is positioned at the rear of the µEDM machine, as illustrated in Fig. 1c for optical microscopic measurement (OMM), characterization, and measurement purposes. It is specifically used to measure the axial and radial wear length of the tool. The measurement accuracy, along with the associated uncertainty, is determined by the resolution and repeatability of the CNC positioning stages, specified as 1 and \pm 15 µm, respectively. Figure 1c also



Fig. 1 Illustration and configuration of the hybrid LBMM– μΕDM integrated setup. a LBMM process in operation. b μΕDM process in operation. c Complete experimental setup



demonstrates the hybrid LBMM-µEDM integrated setup for the experimental work.

2.2 Experimental plan

To study the tool wear characteristics for μEDM in the hybrid process, six sets of experiments, with different work-piece materials (copper and stainless steel) and thicknesses (200 and 600 μm), were conducted. The machining process involved the creation of an array of six LBMM pilot microholes, evenly spaced 1 mm apart in a 3×2 arrangement, followed by fine finishing of through-holes using μEDM with a 300- μm diameter tungsten electrode (as available in the lab). The size of the LBMM pilot hole is critical. If the pilot hole

is too small, it increases the μEDM machining time due to limited access and inefficient material removal. Conversely, if the pilot hole is too large, it results in excessive HAZs, recast layer, and residual spatter, which may affect the final hole quality. Therefore, a suitable LBMM pilot hole size was determined through initial trials to optimize both machining efficiency and hole quality. The selection of LBMM parameters used in this study is described in the following section. Detailed parameters for LBMM and μEDM are tabulated in Table 1. The LBMM process used 75 loops count with a scanning speed of 10 mm/s, a 0° hatch angle, 0.01-mm line spacing, and a 50- μ m focal spot size. A two-way hatch pattern was applied to enhance coverage uniformity and minimize unprocessed areas.



Table 1 LBMM and μEDM parameters

LBMM Parameters				
Loop Count	75			
Programmed Diameter (μm)	180			
Scanning Speed (mm/s)	10			
Laser Rated Power (W)	50			
Actual Measured Laser Rated Power (W)	38.6			
	35.4 (or 90%)			
Applied Laser Power (W)	22 (or 50%)			
	8.62 (or 10%)			
Frequency (Khz)	50			
Hatch Angle (°)	0			
Line Space (mm)	0.01			
Focal Spot Size (µm)	50			
Hatch Type	Two Way Hatch			

μEDM Parameters				
Power Supply Type	Resistor- Capacitor (RC)			
Resistance (K Ω)	1			
Electrode Material	Tungsten			
Electrode Diameter (µm)	300			
Workpiece Material	Copper and Stainless			
	Steel			
Workpiece Thickness (μm)	200 and 600			
Gap Voltage (V)	90			
Capacitance (nF)	10 (1.8 Stray Cap)			
Discharge Energy (μJ)	40.5			
Spindle Speed (RPM)	1200			
Feedrate (µm/s)	5			
Flushing Method	Atmospheric Pressure			
Dielectric Fluid	Mineral based EDM oil			
Polarity	Workpiece: Positive,			
	Tool: Negative			

The electrode was flattened at the bottom before each set of array hole machining to ensure a consistent electrode shape across all sets of microholes. The pregrinding was performed using the block electrical discharge grinding (EDG) method. The influence of flattening the bottom of the electrode on radial wear is not within the scope of this study. However, this step was carried out to eliminate variability in electrode shape and to minimize potential bias in wear measurements. The flatness of the electrode was visually verified using the microscopic camera, and care was taken

to ensure that no significant axial or radial wear was present before machining was performed.

Surface detection was performed for each hole, setting the Z-position to zero and retracting the electrode 100 μm above the surface. To ensure complete cuts through the 200 and 600- μm thickness of workpieces, a programmed depth of 600 and 1000 μm was used, respectively. Using a microscopic camera, images of the microelectrode were captured after each machining hole, allowing for precise measurements of axial and radial wear length. Furthermore,



the machined samples were cleaned with isopropyl alcohol (IPA), followed by cleaning in an ultrasonic bath [38]. A scanning electron microscope (JSM-IT100 from JEOL Ltd.) was used to characterize the machined hole. Third-party software named ImageJ [39] was used for characterization and subsequent measurement purposes.

The selection of workpiece and electrode materials in LBMM-µEDM is important for achieving high precision and efficiency. In µEDM, the electrode material affects the accuracy and shape of the machined microfeatures. Tungsten was chosen as the electrode material due to its high thermal wear resistance and low tool wear rate [40]. In this study, a cylindrical tungsten electrode with a 300-µm diameter was used to ensure consistent machining performance.

For the workpiece, copper and stainless steel (SS) were selected due to their suitability for both EDM and laser machining. Copper was chosen for its high electrical and thermal conductivity, which ensures efficient material removal during µEDM and good laser energy absorption in LBMM. Stainless steel was selected for its high strength, corrosion resistance, and dimensional stability, making it an excellent choice for precision microfabrication. Both materials are commonly used in biomedical devices, aerospace components, industrial filtration, and inkjet nozzles, where microhole arrays require high accuracy, durability, and performance.

2.3 Characterization

This section focuses on the characterization of key performance metrics, including axial and radial wear length measurement methods and hole quality assessment.

2.3.1 Axial and radial wear length measurement

The axial and radial tool wear length (ATWL and RTWL, respectively) was measured using images captured by a microscopic camera after each successive machining process. Axial wear was determined by measuring the distance from the tool's zero reference point, set by the machining coordinate G57, to the initial condition of the electrode tip. Radial wear length, on the other hand, was measured as the distance from the electrode tip to its original, unaltered diameter. Figure 2 illustrates the measurement method for radial and axial wear length on the electrode.

2.3.2 Machining performances

Machining performance is assessed by evaluating the machining time and the quality of machined microholes. In the LBMM process, machining time is recorded in its own graphical user interface (GUI), while for the μEDM process, it is defined as the time required for the electrode to travel

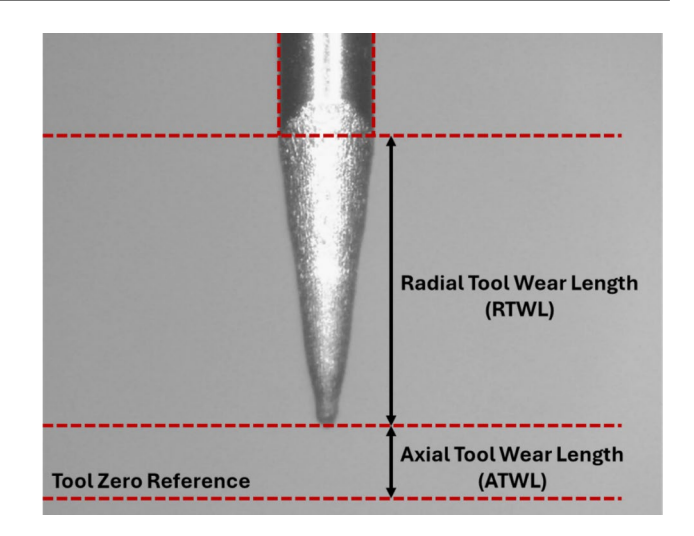


Fig. 2 Measurement of axial and radial wear length

from the workpiece surface to the programmed machining depth. This duration is calculated using Z-axis positional data, which is recorded every 100 ms. The Z-axis positional data also offers insights into the machining progression, enabling the detection of deviations or irregularities during the process. For hybrid machining, the total machining time is the sum of the LBMM and μEDM durations. Figure 3a,b depicts the measurement method for the entry and exit diameters from the SEM images of the copper workpiece, which is essential for taper angle measurement. The same method was applied to the stainless steel workpiece.

Tool wear causes a taperness in the holes during the μ EDM process. The entry hole will have a different diameter than the exit hole. With reference Fig. 3c, the following formula is used to determine the taper angle, θ :

$$\theta = \tan^{-1} \left(\frac{d - b}{2 \cdot h} \right) \tag{1}$$

where d is the entry hole diameter, b is the exit hole diameter, and h is the thickness of the workpiece.

2.4 Study on the selection of LBMM process parameters

The performance of the hybrid LBMM-µEDM process is strongly influenced by key machining parameters from LBMM, including laser power (P), scanning speed (SS), loop count (L), and programmed diameter (PD). For this study, predrilled LBMM holes were used as the initial step to facilitate the subsequent µEDM process. The selection of parameters was guided by their effects on LBMM entry and exit diameters, recast layer area, LBMM processing time, and the final hybrid machining time. Laser power dictates the energy delivered per pulse, scanning speed controls the exposure time on the workpiece, and loop count determines



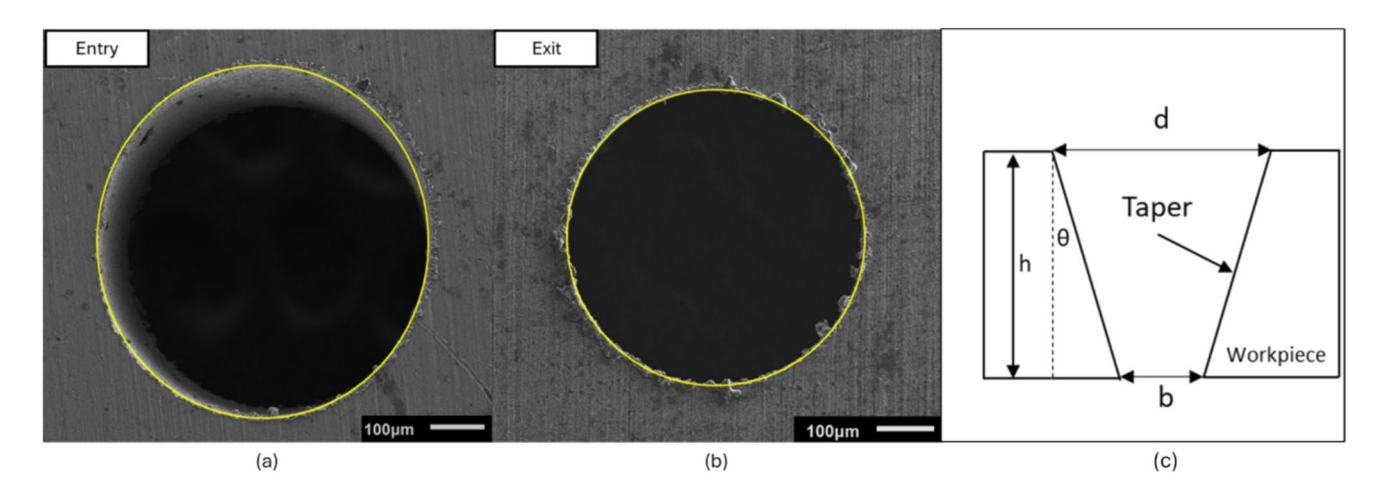


Fig. 3 Diameter (yellow contour) and taper angle measurement of μEDM holes from the SEM images of copper workpiece. a Entry diameter. b Exit diameter. c Taper angle

the total number of laser passes, affecting the cumulative material removal and taper formation. The experiments were carried out on stainless steel workpieces with a thickness of $600 \mu m$. A full factorial experiment was performed using laser powers of 10%, 50%, and 90%, scanning speeds of 10, 100, and $1000 \mu m$, and loop counts of 75, 150, and 225. In a separate study, the programmed diameter was varied with values of 80, 180, and $280 \mu m$.

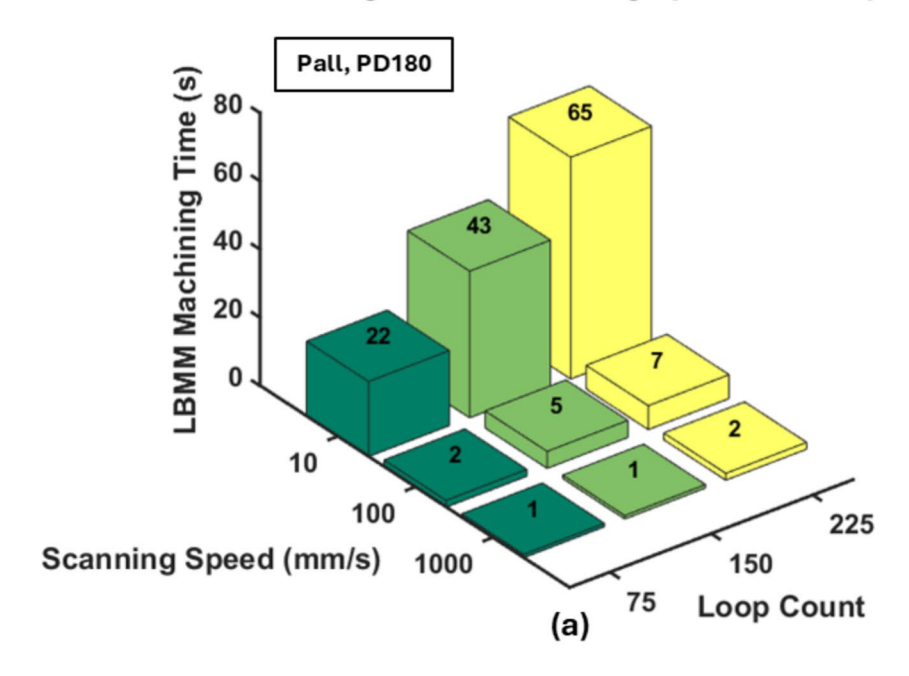
Figure 4a illustrates the effect of scanning speed and loop count on the LBMM processing time for laser powers of 10%, 50%, and 90%, with a programmed diameter of 180 um. It can be observed that processing time decreases significantly with increasing scanning speed, as higher speeds reduce the duration of laser exposure per pass. Higher loop counts, on the other hand, lead to longer laser machining times. For example, at a low scanning speed of 10 mm/s, increasing the loop count from 75 to 225 results in processing times rising from 22 to 65 s. Therefore, a loop count of 75 was selected for this study. Moreover, although very high scanning speeds, such as 1000 mm/s, reduce processing time, they were not chosen because, as shown in Fig. 4b, they result in smaller entry diameters, which would increase the overall machining time in the subsequent µEDM finishing process and will be discussed later. Figure 4b depicts the effect of the power and scanning speed at a fixed loop count of 75 and LBMM programmed diameter of 180 µm. At high power (90%), the largest entry diameters are achieved at low scanning speeds (225 µm at 10 mm/s), with sufficiently large exit diameters to ensure proper debris flow. Ideally, the large entry and exit diameters are preferred, as these through-holes facilitate efficient flushing (during the μEDM finishing process), which is critical for successful hybrid machining. Furthermore, the LBMM programmed diameter has a significant impact on the final hybrid machining performance due to the formation of the recast layer. Importantly, the LBMM entry diameter, including the recast layer, must remain below 300 µm, which corresponds to the μEDM electrode size, to ensure that the recast layer can be fully removed during the subsequent µEDM finishing process. Figure 4c shows the variation of LBMM entry diameter (including and excluding recast layer) and hybrid machining time for different programmed diameters, at 90% laser power, 10 mm/s scanning speed, and a loop count of 75. At a programmed diameter of 80 µm, the hybrid machining time remains relatively long (30 min), similar to the machining time of pure µEDM. In contrast, a programmed diameter of 280 µm results in the fastest hybrid machining time (4 min) and the highest LBMM entry diameter, as the larger diameter improves debris flushing efficiency. However, the LBMM entry diameter, along with the recast layer, is 423 µm, which is larger than the 300-µm electrode used in this study. This leaves part of the recast layer unremoved from the edge of the final hole, resulting in poor hole quality. A typical morphological comparison of the final hole after the hybrid process is illustrated in Fig. 4c, showing the differences between programmed diameters of 180 and 280 µm. The 180-µm hole exhibits complete removal of the recast layer from the edge of the finished hole, while the 280-µm hole still retains some recast material. Therefore, a programmed diameter of 180 µm was selected, as it provides a reasonable machining time of 7 min while maintaining acceptable hole quality. To summarize, the selected LBMM parameters for efficient hybrid machining are 90% laser power, 10 mm/s scanning speed, 75 loops, and a 180-µm programmed diameter. These settings provide sufficient entry and exit diameters for effective flushing, complete removal of the recast layer formation, and balance machining efficiency with hole quality.

Fluence, also known as energy density, refers to the laser energy applied per unit area (J/cm²) during the LBMM process, and cumulative fluence represents the



Fig. 4 a Study of machining time with scanning speed and loop count. Similar trend is observed for all laser power setting. b Effect of laser power and scanning speed on the entry and exit diameters of the LBMMed holes with fixed loop count and programmed diameter. c Effect of programmed diameter on the entry, recast layer size, and hybrid machining time with fixed laser power, scanning speed, and loop count. d Effect of cumulative laser fluence at different laser power on the LBMMed hole's taper angle. e Effect of laser pulse number at different laser power on the LBMMed hole's taper angle

LBMM Machining Time vs Scanning Speed and Loop Count



Entry and Exit Diameter Vs Power and Scanning Speed

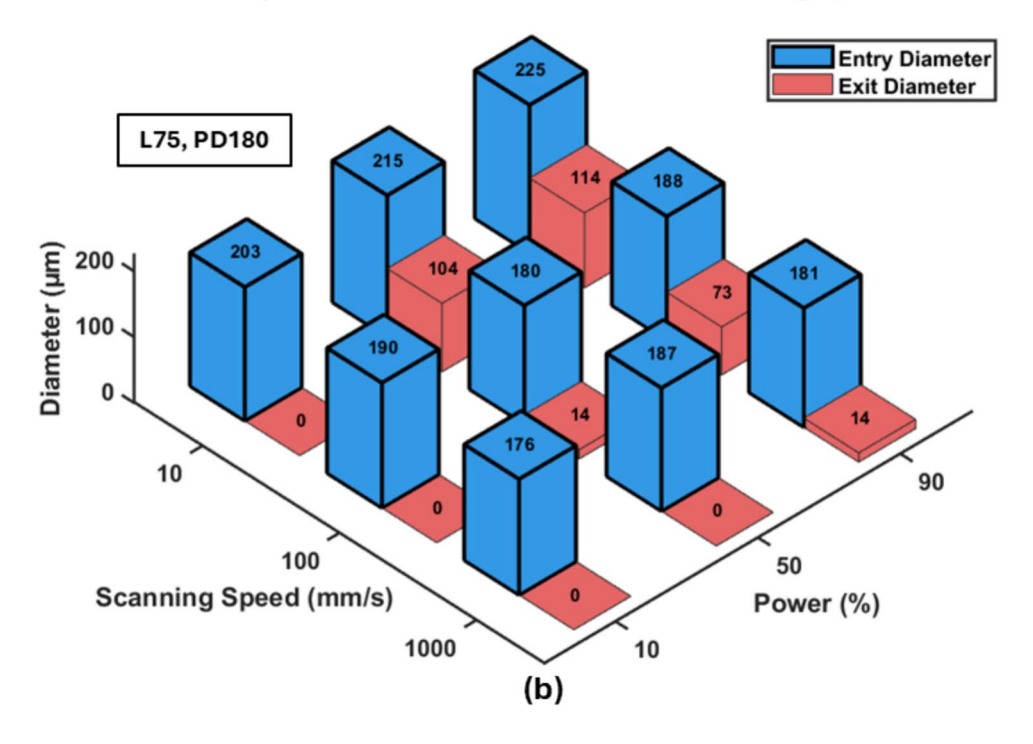
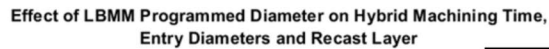
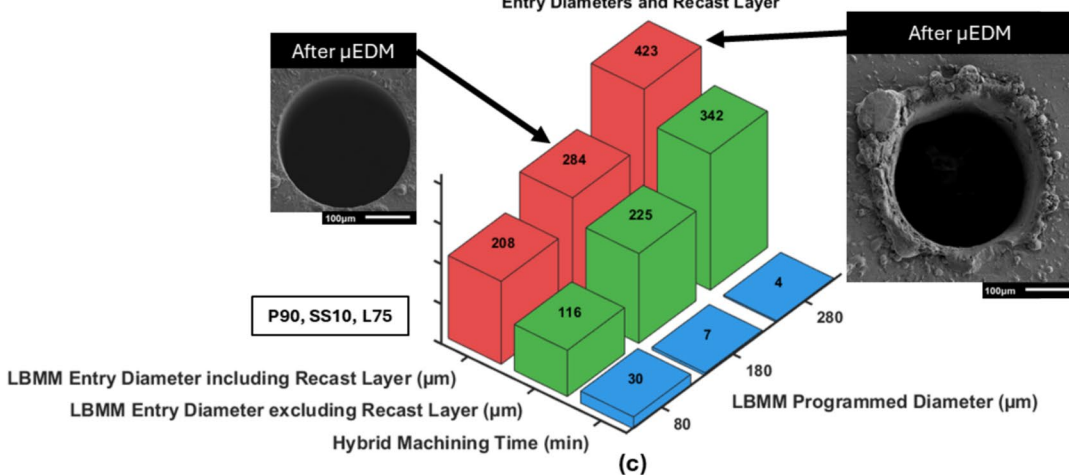
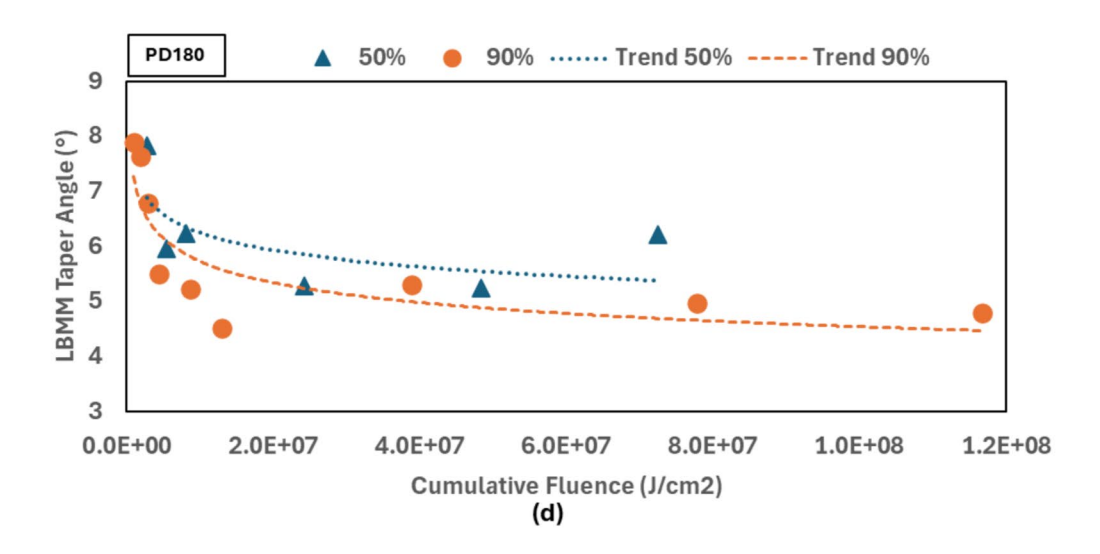


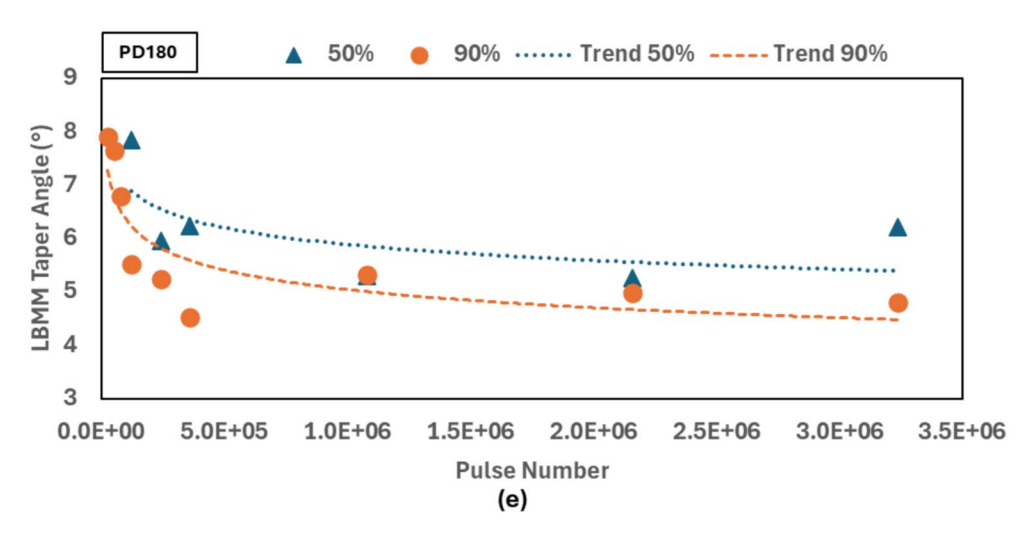


Fig. 4 (continued)











total energy delivered to the material over the entire number of laser pulses. In this study, the cumulative fluence was varied by adjusting the laser power, scanning speed, and loop count. In addition, the pulse number was determined from the laser processing time and laser frequency. The equation for the cumulative fluence is shown in Eq. (2). The effect of the cumulative fluence and laser pulse number on the LBMMed hole's taper angle is shown in Fig. 4d,e, respectively. It should be noted that only LBMMed holes that pierced through were plotted in the figures. LBMMed holes that did not pierce through were excluded, as their taper angle could not be measured. Specifically, at 10% laser power, none of the holes pierced through. At 50% power, the hole at a scanning speed of 225 mm/s did not pierce through. At 90% power, all holes successfully pierced through. It can be inferred from Fig. 4d,e that the taper angle decreases with increasing cumulative fluence and pulse number. At both 50% and 90% laser power, a steep reduction in taper angle is observed at lower fluence and pulse numbers, followed by a gradual decrease that approaches a near-constant value of around 4-5° at higher inputs. Across the entire range, the 90% laser power condition tends to produce lower taper angles compared to 50% power, indicating improved hole quality at higher power settings. This suggests that higher cumulative fluence and larger pulse numbers reduce the diameter difference between the entry and exit holes, thereby minimizing tapering in LBMMed holes. Therefore, 90% laser power was selected in this study, as it resulted in the minimal taper angle along with the largest entry and exit diameters. In the subsequent section, we present the compensation strategy developed to mitigate the effect of the initial taper induced by the LBMM process through subsequent µEDM finishing, which constitutes the primary focus of this study.

Cumulativefluence,
$$F_{cumulative} = \frac{P_{App} \cdot t}{A} \left[\frac{J}{cm^2} \right]$$
 (2)

where P_{App} is the applied laser power (W), t is the processing time (s), and A is the spot area (cm²).

3 Results and discussions

This section presents the results and discussion on tool wear analysis for the µEDM in the hybrid LBMM–µEDM process, with a focus on characterizing axial and radial wear lengths across different workpiece material types and workpiece thicknesses. Additionally, this section outlines a compensation method for tool wear to ensure the fabrication of accurate and consistent microhole arrays.

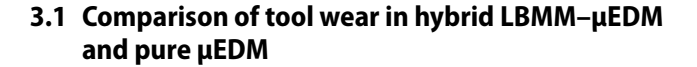


Figure 5a,b illustrates the evolution of electrode geometry during continuous machining on stainless steel material with a thickness of 600 µm for the pure µEDM and hybrid LBMM–µEDM processes, respectively. It can be inferred from Fig. 5a that the electrode subjected to successive pure µEDM experiences more pronounced axial wear while largely maintaining its diameter. In contrast, the electrode used in the hybrid process, as shown in Fig. 5b, develops a tapered, conical shape due to increased radial tool wear length.

This manuscript attempts to explain the different tool wear characteristics observed experimentally for pure µEDM and the LBMM–µEDM process. Figure 6a–d illustrates the spark discharge regions on electrodes during pure µEDM and hybrid laser-based µEDM processes. In Fig. 6a, in pure µEDM, most of the spark discharge occurs at the bottom surface of the electrode as it is positioned above the work-piece. This uniform discharge ensures consistent wear at the bottom. In Fig. 6b, as the electrode machines within the workpiece, the spark discharge is distributed across both the bottom surface and the sidewalls of the electrode. This balanced discharge helps maintain the electrode's shape, minimizes taper, and ensures precise machining.

For the hybrid laser-based µEDM process in Fig. 6c, when the electrode is positioned above the workpiece before penetration, the spark discharge is localized to a small region at the bottom corner of the electrode, with minimal activity at the center of the bottom surface. In Fig. 6d, during machining within the workpiece, the spark discharge is concentrated along the sidewalls of the electrode, promoting radial wear length. This limited discharge activity in the center reduces axial wear, resulting in distinct machining characteristics compared to the pure µEDM process.

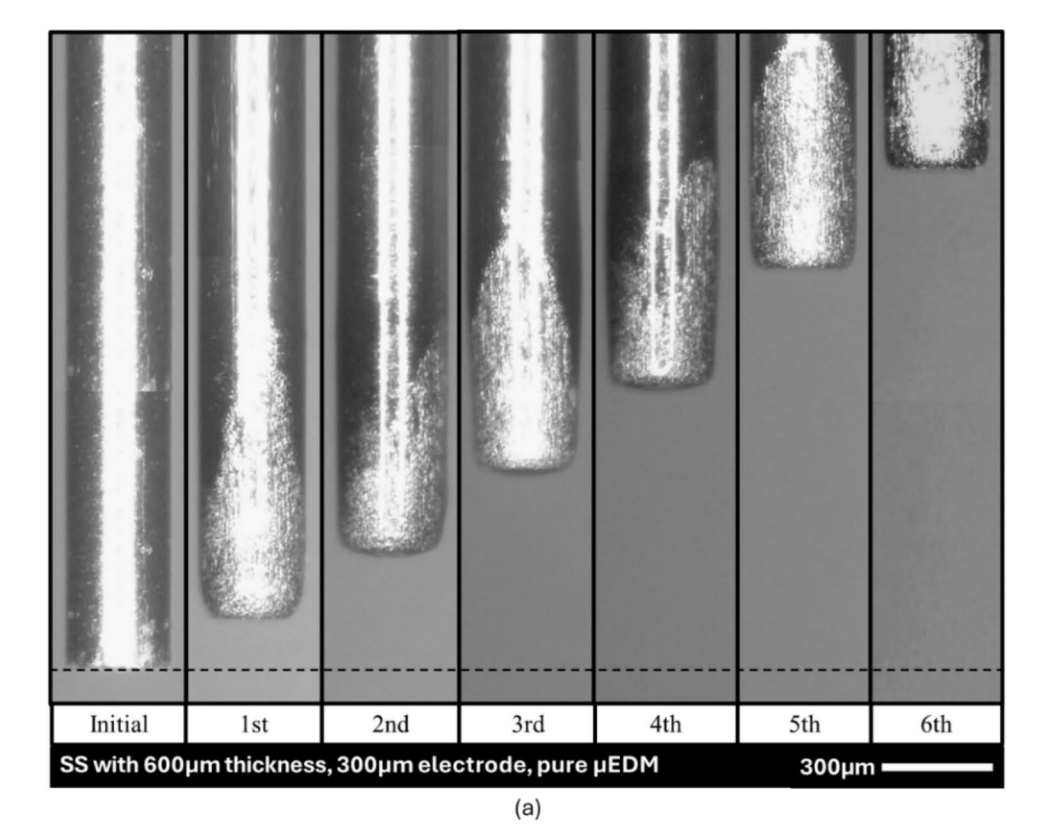
3.2 Comparison of tool wear on different workpiece thickness and material

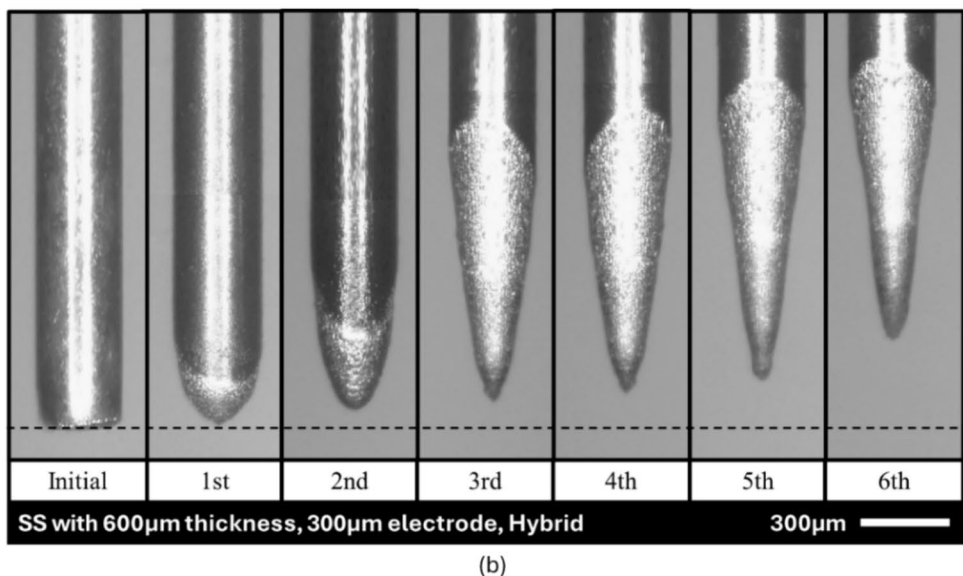
This study investigates the variation in tool wear characteristics when machining stainless steel and copper workpieces with thicknesses of 600 and 200 µm, using a 300-µm electrode in the hybrid LBMM-µEDM process. The evolution of electrode geometry during continuous machining is depicted in Figs. 5 and 7. Based on visual inspection, it can be inferred from the figures that radial wear length is more significant on stainless steel compared to copper. Furthermore, insignificant or no axial wear was observed on the 200-µm thick workpiece (for both copper and stainless steel), in contrast to the 600-µm thick workpiece.

For in-depth analysis, the axial and radial wear lengths during the hybrid LBMM–µEDM, as well as the microhole's



Fig. 5 Evolution of electrode geometry in continuous machining for a pure μΕDM and b hybrid LBMM–μΕDM (stainless steel workpiece of 600-μm thickness with 300-μm electrode)



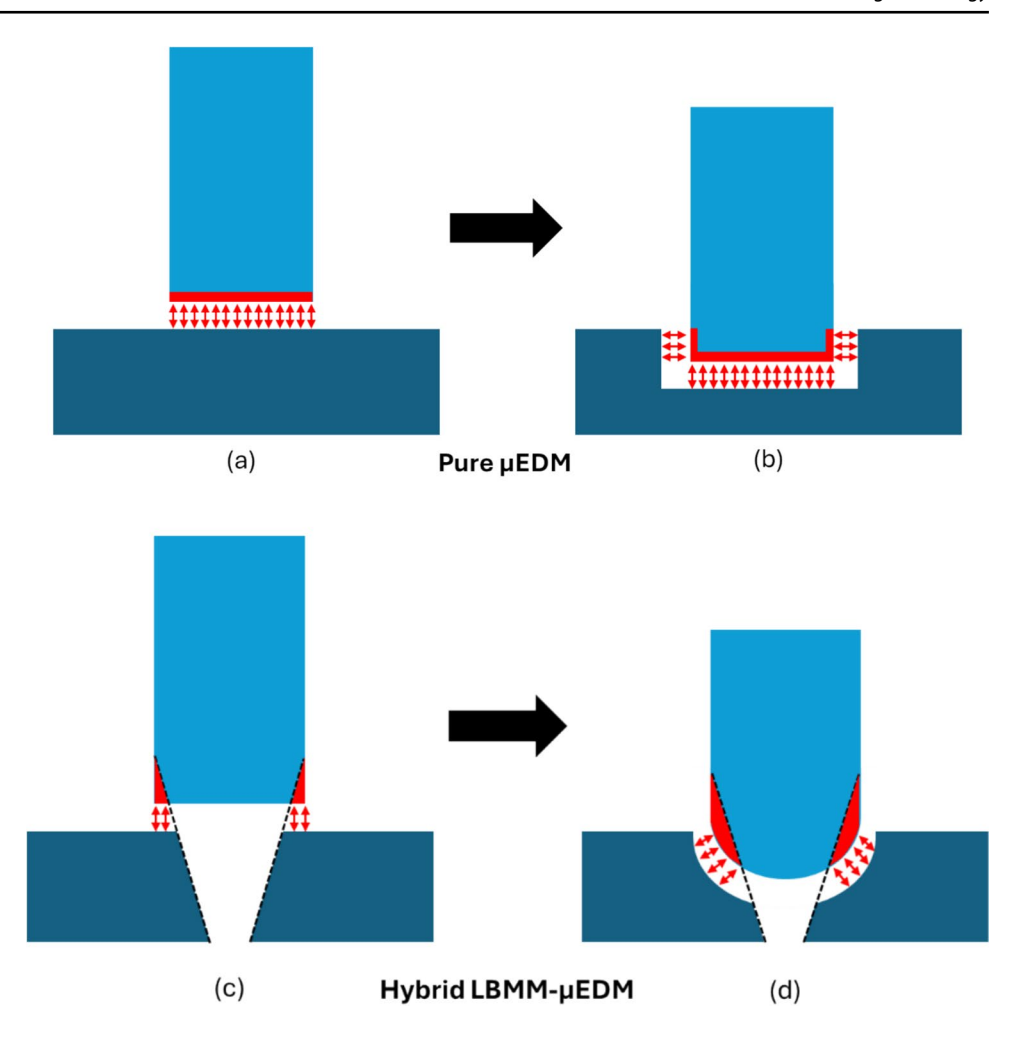


taper angle measurement, are summarized in Fig. 8a-c. Apart from the absence of axial wear on the 200-µm thick workpiece, stainless steel recorded a higher average axial tool wear compared to the copper workpiece in the 600-µm thick workpiece, as shown in Fig. 8a. The reason for this is that the µEDM processing time for copper is much shorter compared to stainless steel, as shown in Fig. 8d. The presence of axial wear in the 600-µm thick workpieces (both stainless steel and copper) but its absence in the 200-µm thick workpieces in Fig. 8a can be attributed to the

differences in machining conditions and spark distribution, as explained in Fig. 6. Thicker workpieces, such as the 600µm ones, require deeper machining, leading to prolonged spark exposure probability on the bottom surface of the electrode, which promotes axial wear. In contrast, the shallower penetration required for the 200-µm thick workpieces reduces the chance of spark exposure on the electrode's bottom surface, effectively almost eliminating axial wear. However, the radial wear length increases continuously with the increase in the hole sequence number, as shown in Fig. 8b



Fig. 6 Spark discharge regions in pure μEDM and hybrid LBMM–μEDM processes. a Electrode positioned above the workpiece before penetration in pure μEDM. b Electrode machining within the workpiece in pure μEDM. c Electrode positioned above the workpiece before penetration in hybrid LBMM–μEDM. d Electrode machining within the workpiece in hybrid LBMM–μEDM



for both materials and thicknesses. Stainless steel, for both thicknesses, shows a higher radial wear length compared to copper. In µEDM machining, copper is widely recognized as an easier material to machine compared to stainless steel [41]. The higher radial wear length observed in stainless steel compared to copper is due to the higher machining time, as depicted in Fig. 8d. The longer interaction time of stainless steel with the electrode contributes to increased tool wear. From a material properties perspective, stainless steel has lower thermal conductivity and a higher melting point than copper, which causes localized heat accumulation and increases the likelihood of wider spark dispersion around the electrode edges, resulting in greater radial wear. Additionally, copper's lower electrical resistivity enables more efficient and frequent spark discharges, resulting in a higher discharge rate and faster material removal. In contrast, the higher electrical resistivity of stainless steel leads to a lower discharge rate, requiring prolonged spark activity to achieve the same depth, thereby increasing tool wear, especially along the radial direction [42].

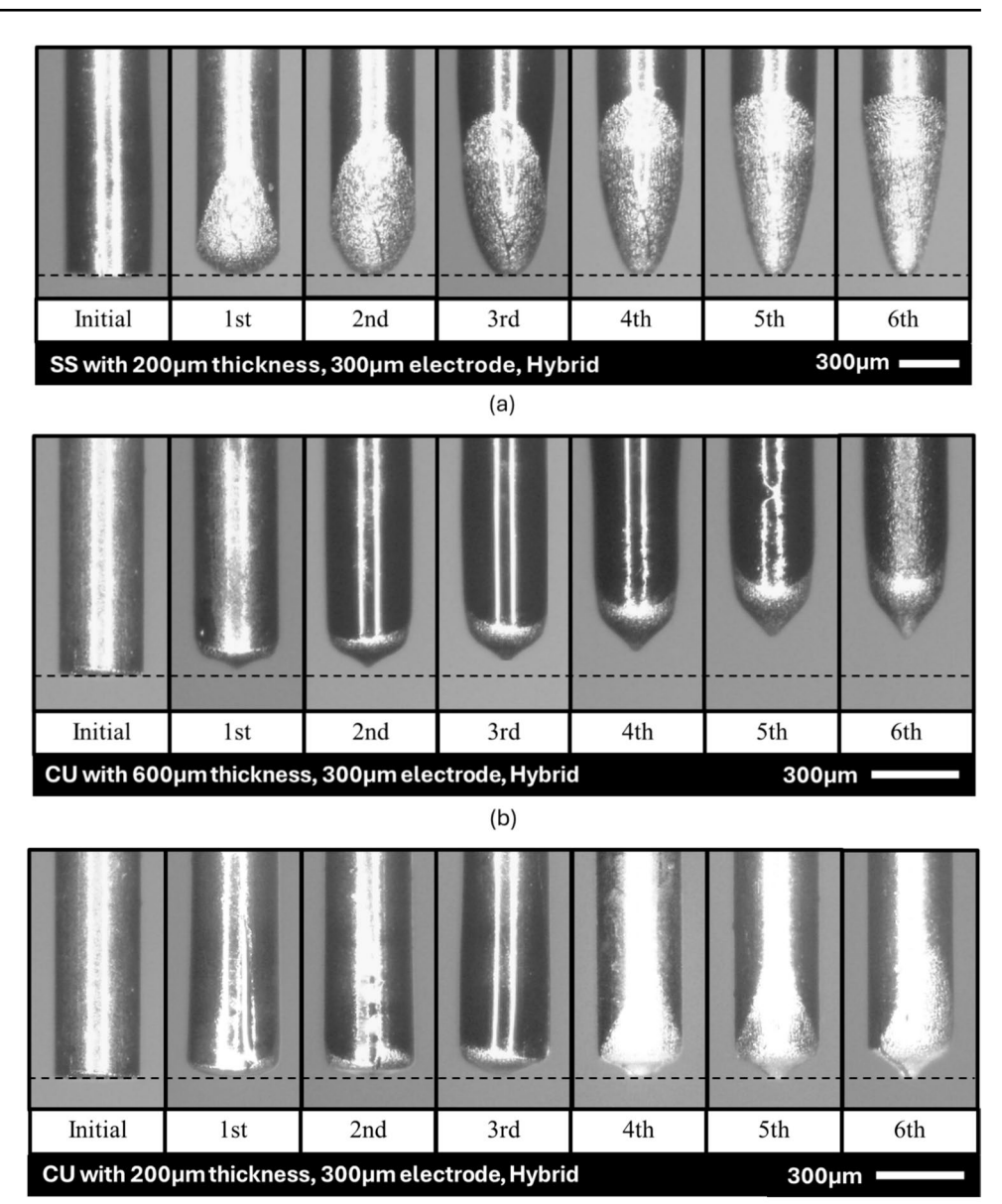
The graph of machining time and discharge pulse number, as shown in Fig. 8d,e, highlights that the 600-µm thick

workpieces have significantly longer machining times and higher discharge pulse numbers compared to the 200-µm thick workpieces. This indicates that the deeper machining required for the 600-µm thickness involves more prolonged spark activity, which contributes to the observed tool wear, axially and radially. However, the increase in machining time is not proportional to the increase in thickness. In hybrid LBMM-µEDM processes, this nonlinear scaling is influenced by several factors. During µEDM, deeper cavities reduce flushing efficiency, causing debris accumulation and unstable discharges, which slow down the MRR [43]. As the machining depth increases, the risk of short circuits and arcing also rises, resulting in more frequent pauses in the process. Moreover, the workpiece thickness has a significant effect on the resulting cut quality during laser machining [44]. This is due to increased laser energy loss as the beam penetrates deeper into the material, where scattering, surface reflection, and thermal diffusion become more pronounced. These combined effects make the machining time grow at a faster rate than the workpiece thickness.

This radial tool wear length directly impacts the tapering of the microhole array, as clearly shown in Fig. 8c. For both



Fig. 7 Evolution of electrode geometry in continuous machining for hybrid LBMM–μEDM for a SS with 200-μm thickness, b Cu with 600-μm thickness, and c Cu with 200-μm thickness (using 300-μm electrode)



(c)

thicknesses of stainless steel, the taper angle increased linearly after successive machining, while copper maintained a consistently low taper angle. Axial wear can be easily compensated for by performing surface detection before machining each hole. However, radial wear length must be compensated for by adjusting the programmed machining depth. In these experiments, the programmed machining depth was set to a constant value for each successive operation: $1000 \, \mu m$ for the $600 \, \mu m$ thick material and $600 \, \mu m$ for the $200 \, \mu m$ thick material, leaving an additional $400 \, \mu m$ to compensate for radial wear. This compensation was sufficient for the copper workpiece, where the maximum radial wear recorded was $335 \, \mu m$, as shown in Fig. 8b, resulting in low taperness in the microholes, as seen in Fig. 8c. However, this was insufficient for the stainless steel material, as the

radial wear length exceeded 400 μm . To address this issue, a dynamic compensation strategy has been proposed, which will be discussed in the next section.

3.3 Compensation strategy and verification

This section proposes an offline compensation method to mitigate the tapering effect in the machining of successive microhole arrays in hybrid LBMM-µEDM. Axial wear is compensated by performing surface detection before machining each hole. However, radial wear length must be compensated by adjusting the programmed machining depth. It is important to clarify that the aim of this study was not to reduce tool wear itself but rather to study its characteristics and propose a compensation strategy to achieve high-quality



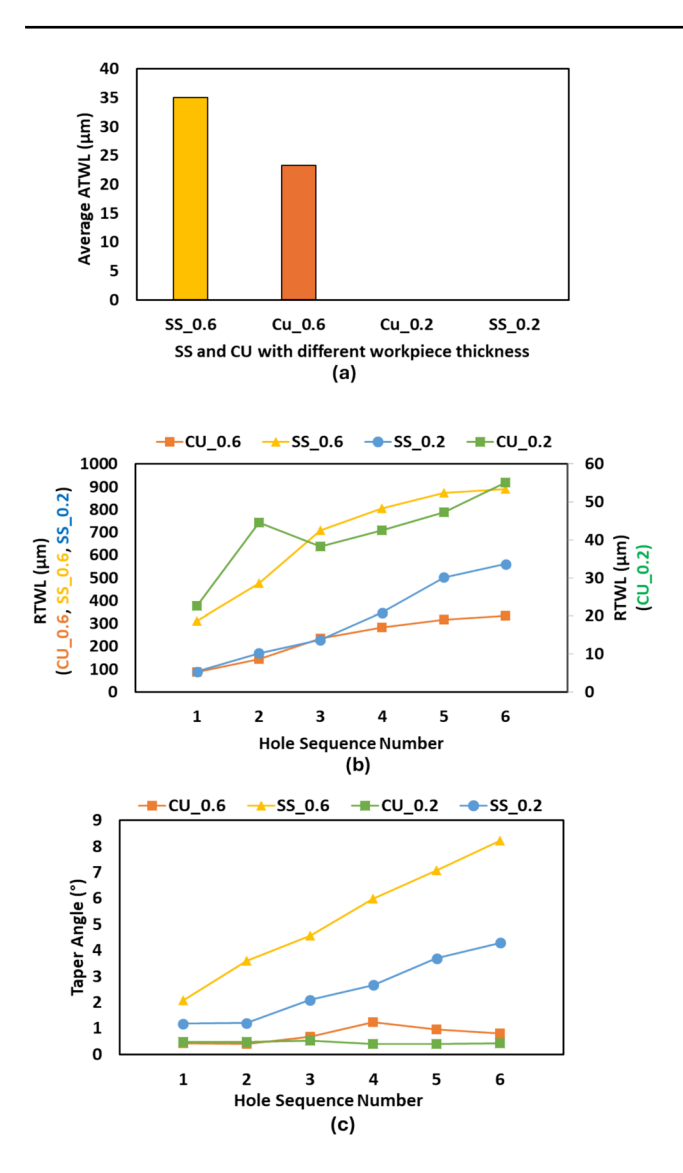


Fig. 8 Comparison of hybrid LBMM-μEDM performance between stainless steel and copper in 600-μm thickness (SS_0.6 and Cu_0.6) and 200-μm thickness (SS_0.2 and Cu_0.2), with 300-μm electrode diameter in terms of **a** average axial tool wear length (ATWL), **b** radial tool wear length (RTWL), **c** microholes' taper angle, **d** machining time, and **e** discharge pulse number

holes with reduced taper angle and efficient machining time. By increasing the programmed machining depth using the proposed dynamic compensation formula, the negative effects of both RTWL and ATWL on the final hole geometry can be significantly minimized. This approach enables more uniform hole profiles and enhances dimensional consistency, despite the inevitable occurrence of tool wear during the process. Moreover, more detailed studies on the effect of laser parameters in sequential LBMM and μEDM processes have been conducted in previous work [45].

Using the experimental data, the radial wear length can be predicted and incorporated into the programmed machining depth calculation. Figure 9a-c illustrates the electrode position during μEDM in the hybrid process with a tapered electrode at different stages: initially, after surface detection, before exiting the workpiece, and after exiting the workpiece.

Initially, the tapered electrode performs surface detection to eliminate the axial wear from the previous hole machining, as shown in Fig. 9a. If the programmed machining depth d is set equal to the workpiece thickness t, the hole will become tapered due to the taper of the electrode, as illustrated in Fig. 9b. To prevent this, the programmed machining depth must be adjusted to account for both the workpiece thickness and radial wear length, with a safety factor f. This factor was introduced to ensure that machining is consistently carried out within the nontapered portion of the electrode, considering several sources of uncertainty in the process. The selected value compensates for uncertainties in radial tool wear length measurement, nonuniform workpiece thickness, surface detection accuracy, and CNC stage positioning, which has a specified tolerance of \pm 15 μ m.

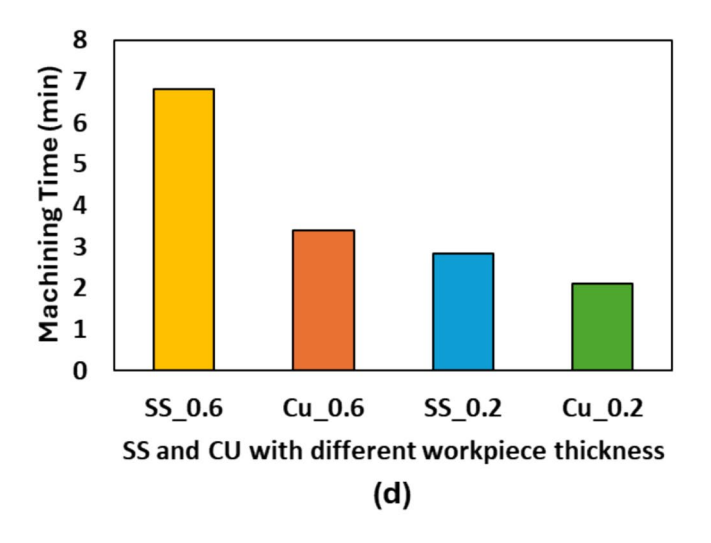
Although the value of f=1.2 was not derived through formal optimization, it was conservatively selected to provide a sufficient safety margin for consistent and reliable throughhole machining. Using a lower value could result in insufficient depth, incomplete breakthrough, or an increased failure rate due to the accumulation of positional and measurement errors. On the other hand, selecting a higher safety factor would unnecessarily increase machining time and may lead to excessive overcutting. Therefore, f=1.2 was adopted as a practical compromise between machining reliability and process efficiency. To ensure consistent through-hole machining and compensate for tool wear and process uncertainties, a depth adjustment strategy is introduced. The programmed machining depth is formulated as in Eq. (3):

$$d_n = f \times (t + RTWL_n) \tag{3}$$

where d_n is the programmed machining depth in micrometer with respect to the hole sequence number n, f is the safety factor, t is the workpiece thickness, and $RTWL_n$ is the radial tool wear length. The radial tool wear length $RTWL_n$ was linearly approximated based on the experimental data, providing a predictive model for adjusting the programmed machining depth, as illustrated in Fig. 9d. Table 2 summarizes the equation for programmed machining depth for stainless steel and copper, considering workpiece thicknesses of 600 and 200 μ m, using a 300- μ m electrode.

The linearized radial tool wear length (RTWL) equation varies based on both the workpiece thickness and the material type, as summarized in Table 2. However, for a given material, the coefficients and constants of the RTWL equations can be estimated through linear interpolation between two known thickness values. For instance, Table 2 presents RTWL equations for stainless steel (SS) at thicknesses of





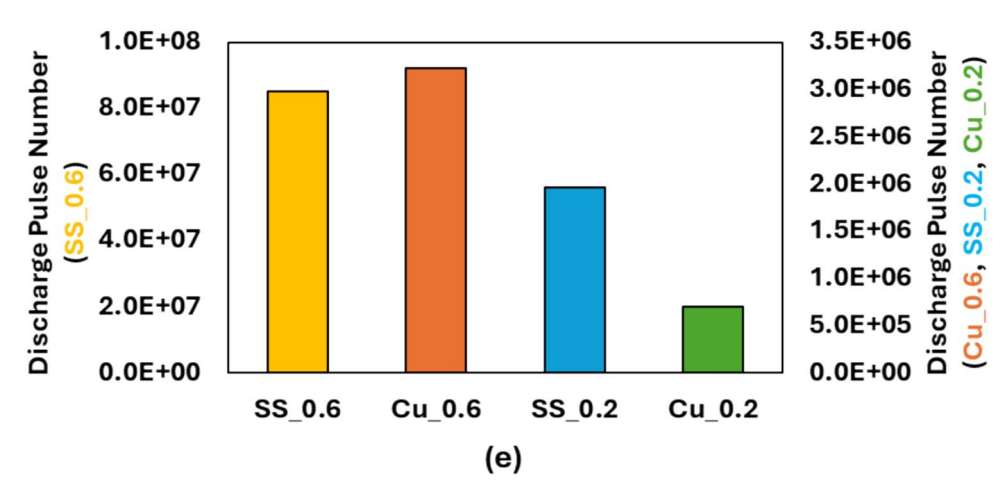


Fig. 8 (continued)

200 and 600 µm. To estimate the RTWL equation for SS at any intermediate thickness within this range, linear interpolation of the coefficient and constant can be employed. The accuracy of the interpolated RTWL equation can be improved by reducing the gap between the experimentally measured thickness values. Another constraint is the available length of the electrode mounted on the collet, which limits the maximum achievable machining depth. Additionally, the model assumes a limited number of holes per electrode, since progressive wear will eventually require repositioning or replacement of the electrode. It is important to highlight that the current RTWL model is specific to the tested material and electrode diameter and therefore may not be directly applicable to other material-electrode combinations. To improve generalizability, a more comprehensive, data-driven approach is recommended. This would involve building a large data set encompassing various workpiece materials, electrode diameters, and machining parameters. Such a dataset could support the development of a universal model using predictive algorithms or machine learning techniques, enabling accurate RTWL estimation across a wider range of conditions.

To verify the compensation strategy, the same experiment was conducted using stainless steel with a thickness of 600 µm and a 300-µm electrode diameter but with the compensation method applied. The safety factor f was set to 1.2. Table 3 compares the programmed machining depth with and without compensation, emphasizing the dynamic adjustment of the programmed depth. From the table, it can be observed that compensation was only possible for the first hole, as the machining depth exceeded both the total radial wear length and the workpiece thickness. However, by employing the proposed compensation method, all radial wear lengths are effectively compensated, as indicated by the green text.

Figure 10 presents a morphological comparison of microhole arrays produced using three different approaches: pure µEDM, hybrid machining without compensation, and



Fig. 9 The electrode position during μEDM in the hybrid process with a tapered electrode. a Initial position after surface detection. b Before exiting the workpiece. c After exiting the workpiece. d Linear approximation of RTWL for stainless steel with a 600- μ m thickness using a 300- μ m electrode

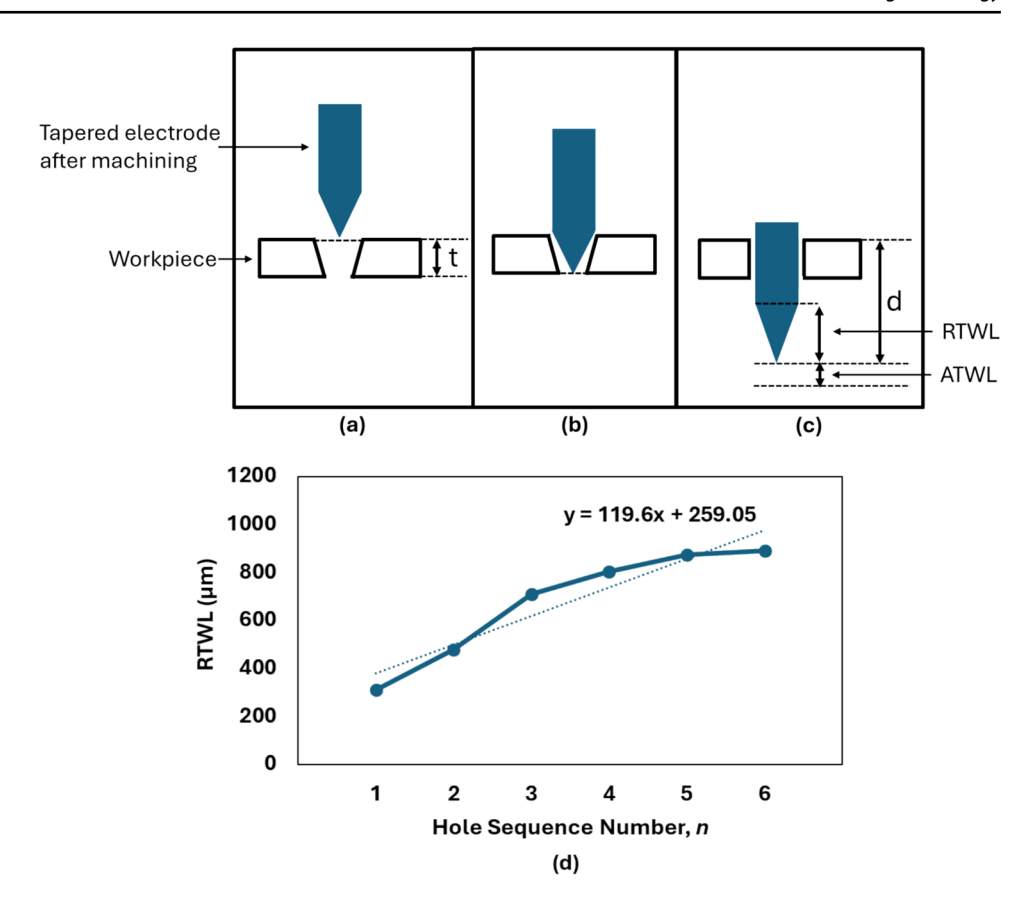


Table 2 Summarized equation for programmed machining depth for stainless steel and copper, considering workpiece thicknesses of 600 and 200 μ m, using a 300- μ m electrode. (t is workpiece thickness, d_n is programmed machining depth, f is the safety factor, and n is the hole sequence number)

t (µm)	Stainless steel	Copper
200	$d_n = f \times (99.156$	$n + 169.928$) $d_n = f \times (6.0012n + 218.759)$
600	$d_n = f \times (119.$	$6n + 859.05) d_n = f \times (51.529n + 653.047)$

hybrid machining with compensation. It is evident that pure μ EDM produces microholes with a minimal taper angle. However, this comes at the expense of longer machining time. To support this observation, Fig. 11 provides a quantitative comparison of machining performance in terms of taper angle and machining time, based on three repeated trials (n=3), with error bars representing the minimum and maximum values. As shown in Fig. 11b, the pure μ EDM approach results in the longest machining time. This tradeoff highlights the advantage of adopting LBMM $-\mu$ EDM, which optimally balances machining speed and precision by leveraging the strengths of both processes. Moreover, as shown in Fig. 11, it is worth noting that the pure μ EDM process exhibits greater variability in machining time, while the

hybrid process without compensation shows higher variability in taper angle, as indicated by the wider range between the minimum and maximum values represented by the error bars.

Furthermore, Fig. 10 also demonstrates that hybrid machining without compensation exhibits a noticeable tapering issue, particularly evident in the exit holes, where the hole size progressively decreases throughout the machining sequence. This phenomenon leads to an increase in taper angle with successive machining, as illustrated in Fig. 11a. In contrast, hybrid machining with compensation effectively addresses this tapering problem, resulting in a lower taper angle that is comparable to that of pure μEDM . On average, the compensation method results in a $7 \times \text{reduction}$ in taper angle compared to the hybrid process without compensation. Additionally, the taper angle in hybrid machining with compensation is $2 \times \text{smaller}$ compared to pure μEDM .

In addition, hybrid machining with compensation exhibits only a slight increase in machining time compared to hybrid machining without compensation. This is primarily due to the need for deeper machining during the compensation process, which adds to the overall machining time. However, both hybrid machining methods are significantly faster than pure µEDM, as shown in Fig. 11b. On average,



Table 3 Programmed machining depth for stainless steel of 600-μm thickness with 300-μm electrode diameter, with and without compensation (green text: compensated)

Hole sequence number, <i>n</i>	RTWL + Workpiece Thickness (µm)	Programmed machining depth, d_n (µm)		
		Without Compensation	With Compensation	
1	912	1000	1174	
2	1076	1000	1318	
3	1309	1000	1461	
4	1404	1000	1605	
5	1475	1000	1748	
6	1491	1000	1892	

the hybrid methods achieve a $4 \times$ reduction in machining time compared to pure μEDM .

In the hybrid process, residual spatters resulting from LBMM are still visible, as shown in Fig. 10. This is primarily because the μ EDM electrode diameter is insufficient to completely remove the spatter during machining. Potential solutions include using a larger μ EDM electrode diameter or

reducing the size of the LBMM hole to ensure better overlap during the finishing process. Additionally, chemical etching has been identified as an effective postprocessing method to further eliminate residual spatter from LBMM and enhance surface quality, as demonstrated in previous studies [46].

These findings confirm that the compensation method effectively mitigates the tapering issue in the successive

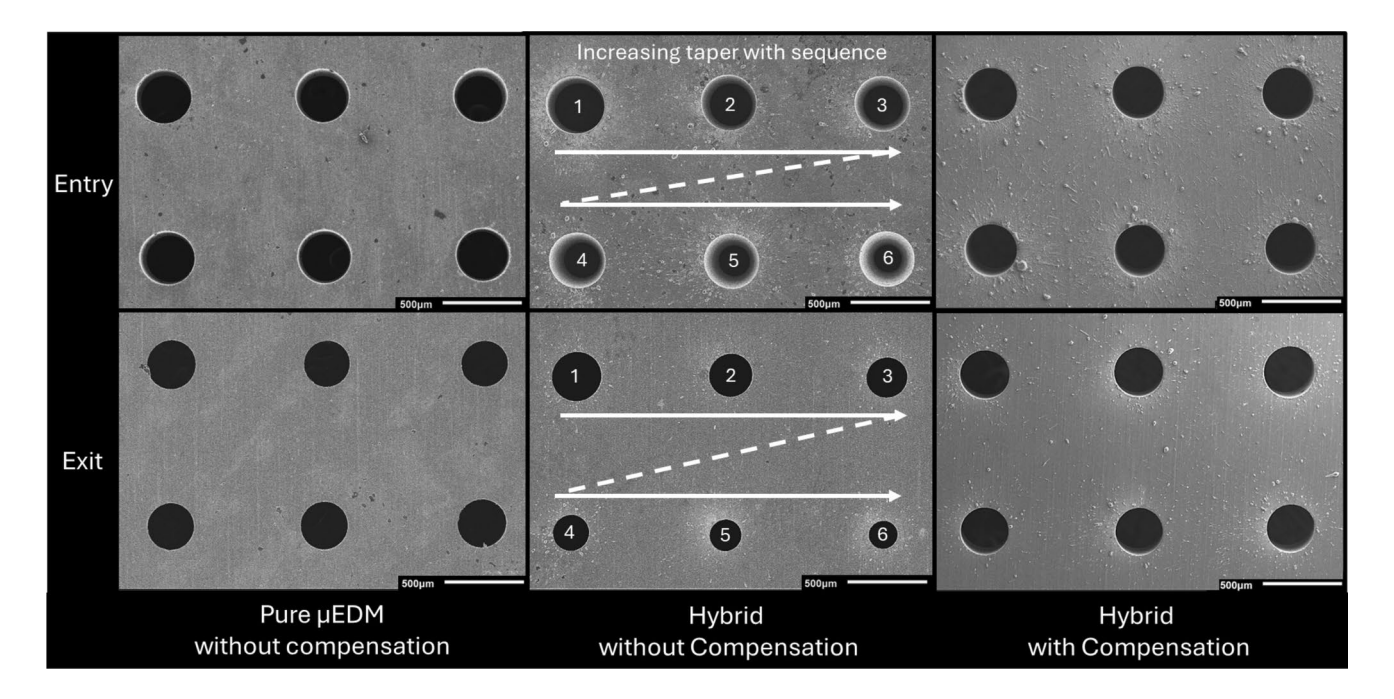
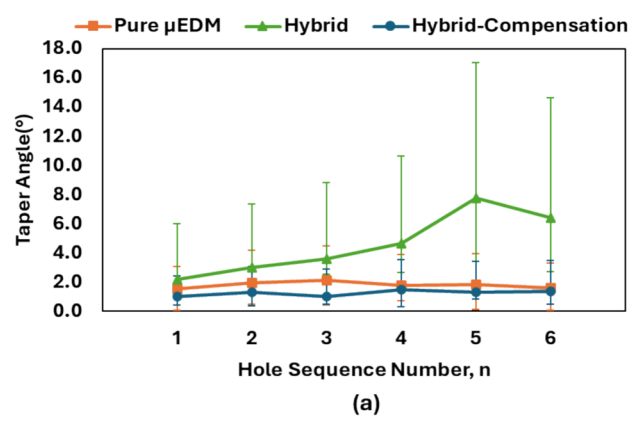


Fig. 10 SEM images showing the morphological comparison of microhole arrays produced by pure µEDM, hybrid without compensation, and hybrid with compensation on a 600-µm thick stainless steel workpiece, highlighting both entry and exit sides for comparison



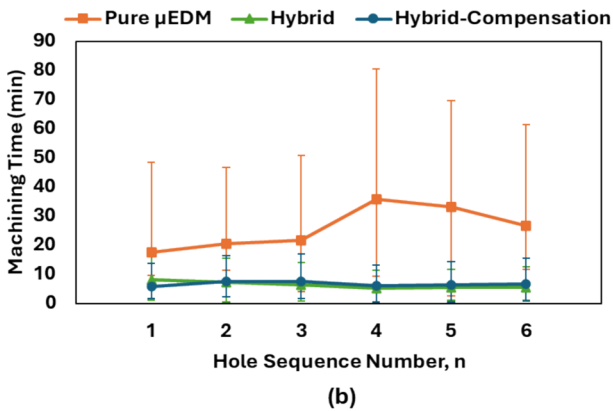


Fig. 11 Comparison of machining performance on 600- μ m thick stainless steel between pure μ EDM, hybrid, and hybrid with compensation, in terms of **a** taper angle and **b** machining time. Error bars represent the minimum and maximum values observed based on three repeated trials (n=3)

machining of microhole arrays by accurately compensating for radial tool wear length.

4 Conclusion

The tool wear analysis for the sequential hybrid LBMM and µEDM process is essential to ensure the practical, consistent, and high-quality fabrication of microhole arrays. As the tool becomes more tapered with each machining step, it can lead to tapered microholes. Key findings from the analysis are as follows:

- The hybrid LBMM-μEDM process exhibited more pronounced radial tool wear length compared to the pure μEDM process, while the pure μEDM process exhibited higher axial tool wear length.
- Stainless steel demonstrated higher radial tool wear length than copper, and thicker workpieces increased axial wear.

- A compensation strategy has been proposed and successfully tested to mitigate the impact of taperness
 and improve the quality of successive microhole array
 machining by adjusting the programmed machining
 depth to account for radial tool wear length, ensuring
 consistent machining quality.
- On average, the hybrid process with compensation results in a 7×reduction in taper angle compared to the hybrid process without compensation. Moreover, the hybrid process with compensation achieves a 4×reduction in machining time compared to pure µEDM.

By effectively compensating for tool wear, the sequential hybrid LBMM- μ EDM process enables the fabrication of microhole arrays with the same high quality as pure μ EDM but at a 4×faster machining rate. This advancement enhances productivity, precision, and sustainability in microfabrication.

Acknowledgements First of all, we thank Allah (SWT) for providing us with the ability to conduct this research. The authors also acknowledge the research support provided by MOHE (Grant No: PRGS/1/2022/TK03/UIAM/02/1) and the International Islamic University Malaysia.

Author contribution WABWA is the research student associated with this work. He conducted all experiments, collected and analyzed the data, and prepared the manuscript. TS served as the project supervisor, providing guidance throughout the research and offering valuable input for manuscript preparation.

Funding Open access funding provided by The Ministry of Higher Education Malaysia and International Islamic University Malaysia This research is also funded under the grant PRGS/1/2022/TK03/ UIAM/02/1 provided by the Ministry of Higher Education, Malaysia. Wan Ahmad Bin Wan Azhar is supported by the KOE IIUM Engineering Merit Scholarship (KOEiems 2023).

Declarations

Competing interests The authors declare no competing interests.

Open Access This article is licensed under a Creative Commons Attribution 4.0 International License, which permits use, sharing, adaptation, distribution and reproduction in any medium or format, as long as you give appropriate credit to the original author(s) and the source, provide a link to the Creative Commons licence, and indicate if changes were made. The images or other third party material in this article are included in the article's Creative Commons licence, unless indicated otherwise in a credit line to the material. If material is not included in the article's Creative Commons licence and your intended use is not permitted by statutory regulation or exceeds the permitted use, you will need to obtain permission directly from the copyright holder. To view a copy of this licence, visit http://creativecommons.org/licenses/by/4.0/.

References

 Li ZY, Wei XT, Guo YB, Sealy MP (2015) State-of-art, challenges, and outlook on manufacturing of cooling holes for turbine



- blades. Mach Sci Technol 19:361–399. https://doi.org/10.1080/10910344.2015.1051543
- Feng J, Qie C, Chen T, Liu H, Zhang Y, Zhang S, Yuan L, Tian Y (2025) Effect of laser frequency and energy on the film cooling holes drilling process of cobalt-based superalloys with thermal barrier coating for aircraft engine blade. Lasers Manuf Mater Process. https://doi.org/10.1007/s40516-025-00300-0
- Gong S, Zhang L, Hu Y, Chan K, Liu J, Wang Z, Wang Y (2025) Micro-holes machining characteristics of Cf-ZrB2-SiC by micro-EDM and taper control based on swing device. Ceram Int 51:10477–10490. https://doi.org/10.1016/j.ceramint.2024.12.480
- Shang J, Ling Y, Ping L, Pan K, Xue Y, Wang Y, Li J, Zhang S, Zhong S (2023) Micro-hole array sprayer combined with an organic membrane to assist LIBS (MASOM-LIBS): a novel highly sensitive detection method for dissolved trace heavy metals in water. Talanta 264:124780. https://doi.org/10.1016/j.talanta.2023. 124780
- Wang C, Lu Z, Zhang K (2018) Fabrication of micro-parts with high-aspect ratio micro-hole array by micro-powder injection molding. Materials 11:1864. https://doi.org/10.3390/ma11101864
- Chen PC, Hsieh SJ, Chen CC, Zou J (2013) A three-dimensional enormous surface area aluminum microneedle array with nanoporous structure. J Nanomater. https://doi.org/10.1155/2013/164953
- Makvandi P, Jamaledin R, Mofidfar M, Wang X, Moon TS (2025) Advances in the development of microarray patches in biomedicine. N Biotechnol 86:25–30. https://doi.org/10.1016/j.nbt.2025. 01.003
- Aralekallu S, Boddula R, Singh V (2023) Development of glassbased microfluidic devices: a review on its fabrication and biologic applications. Mater Des 225:111517. https://doi.org/10. 1016/j.matdes.2022.111517
- Lee US, Sim DB, Lee JH, Kim BH (2024) Fabrication of micro carbon mold for glass-based micro hole array. Micromachines 15:194. https://doi.org/10.3390/mi15020194
- Xin G, Wu C, Liu W, Rong Y, Huang Y (2021) Anti-corrosion superhydrophobic surfaces of Al alloy based on micro-protrusion array structure fabricated by laser direct writing. J Alloys Compd. https://doi.org/10.1016/j.jallcom.2021.160649
- Guo Z, Zhou K, Xiao Y, Jung J-Y, Um H, Moiz SA, Qu S, Liu S, Lee J-H (2011) Silicon microholes array fabricated by femtosecond laser pulses directly writing assisted with further electrochemical etching. In: 2011 37th IEEE Photovoltaic Specialists Conference. IEEE, pp 002870–002873
- Shen SC, Pan CT, Wang YR, Chang CC (2006) Fabrication of integrated nozzle plates for inkjet print head using microinjection process. Sensors and Actuators A: Physical 127:241–247. https://doi.org/10.1016/j.sna.2005.08.016
- Wang Q, Zhang J (2024) Fabrication of RuO2-graphene/graphene thick-and-dense micro-hole array material by femtosecond laser for high volumetric rate performance. Electrochim Acta 504:144919. https://doi.org/10.1016/j.electacta.2024.144919
- Lee C-Y, Lee S-J, Hu Y-C, Shih W-P, Fan W-Y, Chuang C-W (2009) Integration of silicon micro-hole arrays as a gas diffusion layer in a micro-fuel cell. Int J Hydrogen Energy 34:6457–6464. https://doi.org/10.1016/j.ijhydene.2009.05.134
- Chao C-L, Wang W-H, Chao T-M, Chou W-C, Ma K-J (2019) Fabrication of micro-hole array on glass material by abrasive jet machining. IOP Conf Ser Mater Sci Eng 538:012012. https://doi. org/10.1088/1757-899X/538/1/012012
- Xu Z, Wang Y (2021) Electrochemical machining of complex components of aero-engines: developments, trends, and technological advances. Chin J Aeronaut 34:28–53. https://doi.org/10. 1016/j.cia.2019.09.016
- He J, Wang Z, Zhou W, Jian Y, Zhou L (2023) Electrolytic characteristics of microhole array manufacturing using polyacrylamide

- electrolyte in 304 stainless steel. Micromachines 14:1808. https://doi.org/10.3390/mi14101808
- Yung-Chou H (2024) Applying punching without die to microhole array processing. J Manuf Process 116:284–292. https://doi. org/10.1016/j.jmapro.2024.02.064
- Zou Z, Guo Z, Huang Q, Yue T, Liu J, Chen X (2020) Precision EDM of micron-scale diameter hole array using in-process wire electro-discharge grinding high-aspect-ratio microelectrodes. Micromachines 12:17. https://doi.org/10.3390/mi12010017
- Zhang N, Wang M, Ban M, Guo L, Liu W (2024) Femtosecond laser drilling 100 µm diameter micro holes with aspect ratios in a nickel based superalloy. J Mater Res Technol 28:1415–1422. https://doi.org/10.1016/j.jmrt.2023.12.049
- Chavoshi SZ, Luo X (2015) Hybrid micro-machining processes: a review. Precis Eng 41:1–23. https://doi.org/10.1016/j.precisione ng.2015.03.001
- Liu J, Li C, Yang H, Liu J, Wang J, Deng L, Fang L, Yang C (2024) Study on laser-electrochemical hybrid polishing of selective laser melted 316L stainless steel. Micromachines 15:374. https://doi.org/10.3390/mi15030374
- Li L, Diver C, Atkinson J, Giedl-Wagner R, Helml HJ (2006) Sequential laser and EDM micro-drilling for next generation fuel injection nozzle manufacture. CIRP Ann 55:179–182. https://doi. org/10.1016/S0007-8506(07)60393-X
- Kim S, Kim BH, Chung DK, Shin HS, Chu CN (2010) Hybrid micromachining using a nanosecond pulsed laser and micro EDM. J Micromech Microeng. https://doi.org/10.1088/0960-1317/20/1/ 015037
- Al-Ahmari AMA, Rasheed MS, Mohammed MK, Saleh T (2016)
 A hybrid machining process combining micro-EDM and laser beam machining of nickel-titanium-based shape memory alloy.
 Mater Manuf Process 31:447–455. https://doi.org/10.1080/10426 914.2015.1019102
- Antar M, Chantzis D, Marimuthu S, Hayward P (2016) High speed EDM and laser drilling of aerospace alloys. Procedia CIRP 42:526–531. https://doi.org/10.1016/j.procir.2016.02.245
- Hou S, Bai J (2022) Electrode wear prediction and offline compensation for micro-EDM drilling through-hole array using geometry simulation. Int J Adv Manuf Technol 120:6877–6889. https://doi.org/10.1007/s00170-022-09224-x
- Huan L, Jicheng B, Yan C, Guozheng Z, Shaojie H (2020) Micro-electrode wear and compensation to ensure the dimensional consistency accuracy of micro-hole array in micro-EDM drilling. Int J Adv Manuf Technol 111:2653–2665. https://doi.org/10.1007/s00170-020-05811-y
- Bissacco G, Hansen HN, Tristo G, Valentincic J (2011) Feasibility
 of wear compensation in micro EDM milling based on discharge
 counting and discharge population characterization. CIRP Ann
 60:231–234. https://doi.org/10.1016/j.cirp.2011.03.064
- Lauwers B, Kruth J-P, Eeraerts W (2005) Wear behaviour and tool life of wire-EDM-ed and ground carbide punches. CIRP Ann 54:163–166. https://doi.org/10.1016/S0007-8506(07)60074-2
- Kong DZ, Zhang QH, Fu XZ, Zhang Y (2013) Study of electrode wear ratio of piezoelectric self-adaptive micro-EDM. Key Eng Mater 589:505–510. https://doi.org/10.4028/www.scientific.net/ KEM.589-590.505
- Chen Jian, Sun Zhong-Ming, Lu Guo-Dong (2013) Simulation for electrode wear predication in die-sinking EDM based on geometry model. In: 2013 Fifth International Conference on Measuring Technology and Mechatronics Automation. IEEE, pp 1000–1004
- Aligiri E, Yeo SH, Tan PC (2010) A new tool wear compensation method based on real-time estimation of material removal volume in micro-EDM. J Mater Process Technol 210:2292–2303. https:// doi.org/10.1016/j.jmatprotec.2010.08.024
- Chang Y-F, Chiu Z-H (2004) Electrode wear-compensation of electric discharge scanning process using a robust gap-control.



- Mechatronics 14:1121–1139. https://doi.org/10.1016/j.mechatronics.2004.06.005
- 35. Yan M-T, Lin S-S (2011) Process planning and electrode wear compensation for 3D micro-EDM. Int J Adv Manuf Technol 53:209–219. https://doi.org/10.1007/s00170-010-2827-8
- Ravasio C, Pellegrini G (2025) Experimental investigation on micro-EDM hybrid drilling process. Adv Ind Manuf Eng 10:100155. https://doi.org/10.1016/j.aime.2024.100155
- 37. Bin Wan Azhar WA, Saleh T (2024) Conceptualization of a hybrid machine combining laser beam micro machining (LBMM) and micro electrical discharge machining (micro-EDM) in a single setup. In: 2024 9th International Conference on Mechatronics Engineering (ICOM). IEEE, pp 316–321
- 38. Schaeffer RD, Kardos G (2008) Post-laser processing cleaning techniques | industrial laser solutions.
- Schneider CA, Rasband WS, Eliceiri KW (2012) NIH image to ImageJ: 25 years of image analysis. Nat Methods 9:671–675. https://doi.org/10.1038/nmeth.2089
- Raju L, Hiremath SS (2016) A state-of-the-art review on micro electro-discharge machining. Procedia Technol 25:1281–1288. https://doi.org/10.1016/j.protcy.2016.08.222
- Mahardika M, Tsujimoto T, Mitsui K (2008) A new approach on the determination of ease of machining by EDM processes. Int J Mach Tools Manuf 48:746–760. https://doi.org/10.1016/j.ijmac htools.2007.12.012
- 42. Wan Azhar WA, Bin ST, Razib MABM (2022) Application of CANFIS for modelling and predicting multiple output

- performances for different materials in μEDM. CIRP J Manuf Sci Technol 37:528–546. https://doi.org/10.1016/j.cirpj.2022.02.
- Liu Y, Chang H, Zhang W, Ma F, Sha Z, Zhang S (2018) A simulation study of debris removal process in ultrasonic vibration assisted electrical discharge machining (EDM) of deep holes †. Micromachines 9:378. https://doi.org/10.3390/mi9080378
- Keles O, Oner U (2012) Laser cutting process: influence of workpiece thickness and laser pulse frequency on the cut quality. Arab J Sci Eng 37:2277–2286. https://doi.org/10.1007/ s13369-012-0306-2
- Rashid MAN, Saleh T, Noor WI, Ali MSM (2021) Effect of laser parameters on sequential laser beam micromachining and micro electro-discharge machining. Int J Adv Manuf Technol 114:709– 723. https://doi.org/10.1007/s00170-021-06908-8
- Demir AG, Previtali B, Bestetti M (2010) Removal of spatter by chemical etching after microdrilling with high productivity fiber laser. Phys Procedia 5:317–326. https://doi.org/10.1016/j.phpro. 2010.08.152

Publisher's Note Springer Nature remains neutral with regard to jurisdictional claims in published maps and institutional affiliations.

